Exp Fluids (2016) 57:8
DOI 10.1007/s00348-015-2096-2

RESEARCH ARTICLE

Experimental study on instantaneous thrust and lift of two plunging wings in tandem

Wu Qi Gong[1] · Bo Bo Jia[1] · Guang Xi[1]

Received: 16 July 2015 / Revised: 4 December 2015 / Accepted: 8 December 2015 / Published online: 24 December 2015

Abstract Two tandem wings undergoing a two-dimensional sinusoidal plunging motion are studied in a low Reynolds number water tunnel. The influence of the phase angle and leading-edge vortex (LEV) on the peak value of the instantaneous thrust and lift is studied. The instantaneous lift and thrust are measured by a force sensor; the velocity and vorticity fields are captured by digital particle image velocimetry. For the forewing, noticeable differences at various phase angles are found in the peak value of the instantaneous lift and thrust rather than in their minimum value. The LEV of the hindwing increased the maximum effective angle of attack of the forewing and enhanced the jet-like flow behind the forewing, which accounts for the increase in peak value. For the hindwing, the phase angle determines the sign of the forewing-shed LEV when the hindwing encounters this LEV. If the forewing-shed LEV before the leading edge of the hindwing has the opposite sense of rotation as the LEV of the hindwing, the velocity of the flow on the windward side of the hindwing increases, resulting in high instantaneous thrust and lift. If the two LEVs have the same sense of rotation, the forewing-shed LEV hinders the growth of the hindwing LEV because of the small effective angle of attack, leading to low instantaneous thrust and lift. Non-circulatory forces on the wings are calculated according to a potential flow model. Results show that the non-circulatory force has important effects on the peak value and symmetry of the instantaneous lift and thrust curves.

✉ Wu Qi Gong
wqgong@mail.xjtu.edu.cn

[1] Department of Fluid Machinery, School of Energy and Power Engineering, Xi'an Jiaotong University, Xi'an 710049, Shaanxi Province, People's Republic of China

List of symbols

C	Wing chord length (m)
c_t	Instantaneous thrust coefficient
c_l	Instantaneous lift coefficient
C_T	Mean thrust coefficient
f	Plunging frequency (Hz)
h	Non-dimensional plunging amplitude (h_0/c)
h_0	Plunging amplitude (m)
Re	Reynolds number ($Re = U_\infty\, c/\nu$)
s	Wing span length (m)
St	Strouhal number ($St = f\, A/U_\infty$)
t	Time (s)
T_0	Plunging period (s)
U_∞	Free stream velocity (m/s)
$\alpha(t)$	Nominal angle of attack (°)
α_{eff}	Effective angle of attack (°)
φ	Phase angle between the plunging motions of the forewing and hindwing (°)
ν	Fluid kinematic viscosity (m^2/s)
ρ	Fluid density (kg/m^3)
Ω	Vorticity magnitude, $\Omega = \partial v/\partial x - \partial u/\partial y$ (s^{-1})

1 Introduction

Tandem wing configurations found among nature's flyers have several benefits (Alexander 1984; Platzer et al. 2008; Usherwood and Lehmann 2008; Lehmann 2008). For example, dragonflies can adjust the phase angle between the flapping motion of their forewing and hindwing to attain speeds of up to 10 m/s and instantaneous accelerations of up to 4 g (Alexander 1984). The observation that adjusting the phase angle can realize superior aerodynamic performance is helpful in building micro-air vehicles (MAVs) with tandem wing configurations operating at similar Reynolds numbers (Re).

Dragonflies rely heavily on the complex interaction of vortices to provide high lift and thrust as opposed to the steady-state flow dynamics utilized by fixed wings (Jones and Platzer 1997; Platzer et al. 2008; Lian et al. 2014). The behavior of the vortices is always associated with the adjustment of the phase angle. Therefore, phase angle is an important study object for experimental investigations (Saharon and Luttges 1987, 1988, 1989; Maybury and Lehmann 2004; Yamamoto and Isogai 2005; Wang and Russell 2007; Wang et al. 2003; Warkentin and DeLaurier 2007; Lehmann 2008; Usherwood and Lehmann 2008) or numerical investigations (Jones and Platzer 1997; Sun and Lan 2004; Akhtar et al. 2007; Broering et al. 2010, 2012; Dong and Liang 2010; Lian et al. 2014).

Yamamoto and Isogai (2005) examined the interaction between the forewing and hindwing during hovering flight when the phase angle is 0–90°. It was found that the phase angle has a small effect on the mean forces of the forewing and hindwing. Maybury and Lehmann (2004) found that in hovering flight the performance of the forewing remains approximately constant, whereas the performance of the hindwing is closely associated with the phase angle. They suggested increasing the angle of attack and magnitude of the local flow could increase the lift. These studies (Yamamoto and Isogai 2005; Maybury and Lehmann 2004) indicated that the effect of phase angles on the forewing seems unobvious in hovering flight. In forward flight, Warkentin and DeLaurier (2007) presented a systematic study of the mean thrusts, lifts, and propulsive efficiencies of single and tandem flapping membrane wings when the phase angle is 0–360° under controlled wind-tunnel conditions. They found that a tandem arrangement can increase the mean thrust relative to two single wings at certain phase angles.

The phase angle affecting the lift and thrust is linked to the interaction of the vortices between the forewing and hindwing (Maybury and Lehmann 2004 ; Akhtar et al. 2007; Broering et al. 2012). Broering and Lian (2012) suggested that phase angle affects the time instant of the interaction between the forewing-shed leading-edge vortex (LEV) and the hindwing LEV. The forewing-shed LEV can change the generation and shedding process of the hindwing LEV and alter the instantaneous force of the hindwing compared with that of the single wing. These numerical studies mainly focused on how the forewing-shed LEV affects the hindwing (Broering et al. 2010, 2012; Broering and Lian 2012).

Although real dragonflies do flap their wings using not only a plunging motion, the plunging motion is selected for study. The real flapping motion is three dimensional (3-D); however, previous studies have shown that two-dimensional (2-D) models can reveal some salient features of 3-D flow (Lua et al. 2011). The salient feature of the flow for two closely situated wings is the interaction between the forewing and the hindwing LEVs (Lian et al. 2014). The present 2-D study does not intend to analyze the interaction between the LEV and the spanwise flow, but the interaction between the forewing and hindwing LEVs.

The measured instantaneous lift and thrust include the non-circulatory (added mass) forces for the plunging motion. The added mass force is dependent on the acceleration and is especially important near stoke reversal (Minotti 2002). It is unclear exactly what proportion of the lift and thrust is due to circulatory as opposed to non-circulatory forces for the unsteady flow over two tandem flapping wings. In order to study the effect of the LEV or circulatory force on the lift and thrust, it is necessary to remove the added mass force from the measured results. Ford and Babinsky (2013) developed a two-dimensional potential flow model of the impulsively started flat plate aerofoil to separate the contributions of non-circulatory lift to the total lift. The present paper applies the potential model to calculate the non-circulatory force.

Gong et al. (2015) measured the mean thrust of the two-dimensional plunging forewing and hindwing when phase angle changes from 0 to 360° and spacing distance varies from 0.5 to 2.5 c, where c is the chord length. Their study showed that there is an intense interaction between the forewing and hindwing. In a certain phase angle, the mean thrust coefficients of the forewing and hindwing are significantly greater than the value of a single wing. However, in that paper the production mechanism of the peak value of the instantaneous thrust is not paid much attention, which determines the value of the mean thrust. The present paper tries to answer how the peak or magnitude value of the instantaneous thrust and lift is influenced by the phase angle and LEV of the forewing and hindwing. In order to answer what proportion of the lift and thrust is due to circulatory as opposed to non-circulatory forces for the unsteady flow over two tandem plunging wings, the paper calculates and discusses the added mass force generated by a single plunging wing.

An experimental study is performed in a low Re water tunnel for two tandem wings undergoing 2-D sinusoidal plunging motion. The instantaneous lift and thrust on the forewing and the hindwing are measured by a three-component Kistler force sensor; the vorticity and relative velocity vector field around the wings are measured by digital particle imaging velocimetry (DPIV). Test method is described in Sect. 2. The influencing mechanism of the LEV on the peak value of the instantaneous thrust and lift is discussed in Sects. 3.2 and 3.3. The contributions of the non-circulatory force to the total lift and thrust are studied in Sect. 3.4.

2 Experimental setup and procedure

2.1 Water tunnel and wing motion system

Experiments were carried out using an integrated facility in a recirculating water tunnel at the School of Energy and Power Engineering, Xi'an Jiaotong University. The integrated facility consists of a 2-D plunging wing mechanism, a force measurement system, and a DPIV system (Fig. 1). The test section of this low-speed water tunnel has a cross section of 300 × 300 mm and a length of 1500 mm. Free stream velocity U_∞ in the test section was held constant at 0.2 m/s, with an error of 0.01 m/s; the corresponding turbulent intensity is less than 3.0 %. For a detailed description of the water tunnel, please refer to Gong et al. (2015).

The plunging wing mechanism sits on top of the test section. The forewing and the hindwing are positioned vertically in the test section to mimic a forward flight. The fixed spacing distance between both wings is a half chord length. They both have a NACA 0012 section, and their chord and spanwise lengths are 50 and 260 mm, respectively. The chord-based *Re* was approximately 10^4. The plunging motion of each wing was controlled by a servomotor, which drives a set of eccentric wheel and slider mechanism that converts the rotational motion of the servomotor into a translational motion of the wing. Thus, the phase angle between the forewing and the hindwing was adjusted by controlling the interval between the starting times of the two servomotors. The adjustment error of the phase angle was ±0.5°.

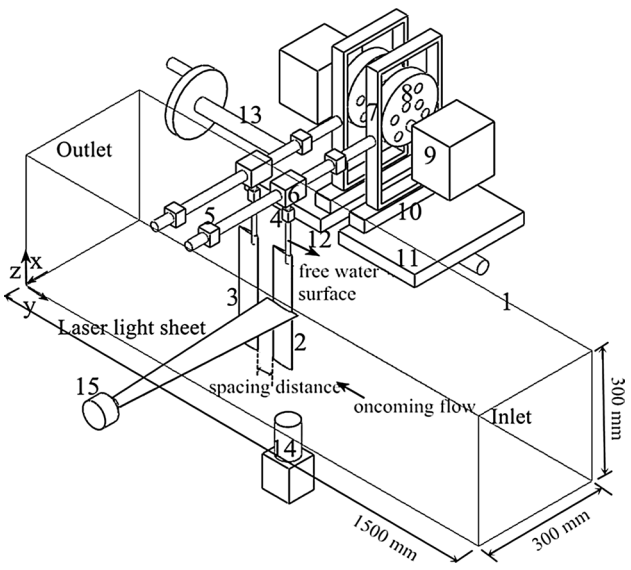

Fig. 1 Side view of the experimental configuration. The wing plunges in and out of the page. *1* Test section of the water tunnel; *2* forewing (FW); *3* hindwing (HW); *4* force sensor; *5* sliding support; *6* connection block; *7* carriage; *8* eccentric wheel; *9* servomotor; *10* sliding chute; *11* forewing base; *12* hindwing base; *13* screw rod; *14* CCD camera of DPIV; and *15* cylindrical lens of DPIV

The clearance between the low end of the wing and the bottom surface of the test section was 4 mm. Dye visualization (Anderson et al. 1998) showed that the end effects can be significantly reduced with such a small clearance. The upper end of the wing was about 25 mm away from the free water surface. This distance was estimated to minimize the adverse effects of free water surface on instantaneous force on the plunging wing through tests. The flow in the mid-span region of the wing was 2-D, with no visible spanwise motion. The distance between the wing and the sidewall of the test section was approximately 115 mm when the plunging wing was located at the peak deviation; the ground effects can be negligible.

2.2 Force and flow field measurement

Forces on the wing were measured using a Kistler piezoelectric three-component force sensor (Kistler, Type 9317B). The force sensor was first calibrated with counterweights using a static unloading calibration method. A linear relationship between the force on the sensor and the output voltage was obtained. The error in the measured forces (by the sensor) was less than 1.5 % of the applied weight (a known weight). The combined inertia of the wing and sensor was measured by repeating the same plunging motion in air, and the forces measured were then subtracted from the corresponding forces obtained in water. However, the effect of inertia on the results was negligible.

Force data acquisition programs were developed based on the NI LabVIEW platform. Data acquisition started after the first 10 plunging cycles and ended before the final 10 cycles to avoid inertial start and stopping effects. Data were acquainted at a sampling rate of 1000 Hz for at least ten successive cycles and thus were averaged over ten cycles. Force data acquisition for each case was repeated three times to improve reliability.

The flow field around the wing was measured using a 2-D TSI DPIV system. A CCD camera (1024 × 1024 pixels) was placed under the test section and perpendicular to a laser light sheet (1 mm thickness) that illuminates a horizontal measurement plane through the cross section of the wing, as shown in Fig. 1. The flow-tracing particle was SiC with a nominal mean diameter of 1.5 μm, whose response time was approximately 0.26×10^{-6} s in our experiments. This response time was much smaller than the timescale of the free stream. Therefore, the SiC particle can follow the flow faithfully.

In the image processing, each rectangular interrogation window had 32 × 32 pixels with 50 % overlap. The area of each particle image was 43 mm × 43 mm, and the spacing resolution of the velocity vector fields was 0.0134 *c*. To reflect the complete flow field around the wing (the chord

length of 50 mm), the flow field around one wing was divided into two segments, their respective images were obtained, and the two corresponding flow images were stitched together.

Digital particle imaging velocimetry uncertainties include random and bias errors in the velocity measurements (Lua et al. 2011). The sub-pixel resolution was around 0.1 pixels, and the corresponding resolution of the velocity measurement in the present experiment was 16.8×10^{-3} m/s (=43 mm/1024 × 0.1/250 μs), where 250 μs is the time interval between the two adjacent particle images. Thus, the uncertainty caused by a random error relative to the maximum flow velocity of 0.43 m/s in the experiment was about 3.9 %. The primary source of bias error in the PIV velocities was attributed to the uncertainty in image scaling (Lua et al. 2011), which had less than 0.1 % error. Therefore, the combination of random and bias errors was approximately 4.0 %.

2.3 Kinematic equation of the wing

The forewing and hindwing were oscillated with a pure plunging motion based on a simple harmonic motion:

$$\text{Forewing: } x(t) = h_0 \sin(2\pi ft) \tag{1}$$

$$\text{Hindwing: } x(t) = h_0 \sin(2\pi ft - \varphi) \tag{2}$$

where h_0 is the plunging amplitude, which refers to the maximum distance deviating from equilibrium position, and φ is the phase angle by which the forewing leads the hindwing in each plunging cycle. The reduced frequency k was defined as follows:

$$k = \pi fc/U_\infty \tag{3}$$

where U_∞ is the free stream velocity. Plunging frequency f was fixed at 1.0 Hz; thus, k was 0.785. The Strouhal number St was calculated as follows:

$$St = 2fh_0/U_\infty \tag{4}$$

Taylor et al. (2003) showed that the Strouhal number of 42 different species of bats, birds, and insects in cruise flight was within a narrow range of $0.2 < St < 0.4$, with an average value of 0.29. In the present study, the non-dimensional plunging amplitude h_0/c was 0.7, which corresponded to $St = 0.35$.

Thrust T and lift L were defined as forces normal and parallel to the plunging motion, respectively, as shown in Fig. 2. The instantaneous thrust c_t and lift c_l coefficients of the forewing or hindwing were defined as follows:

$$c_t = \frac{\hat{T}(t)}{0.5\rho U_\infty^2 cs} \tag{5}$$

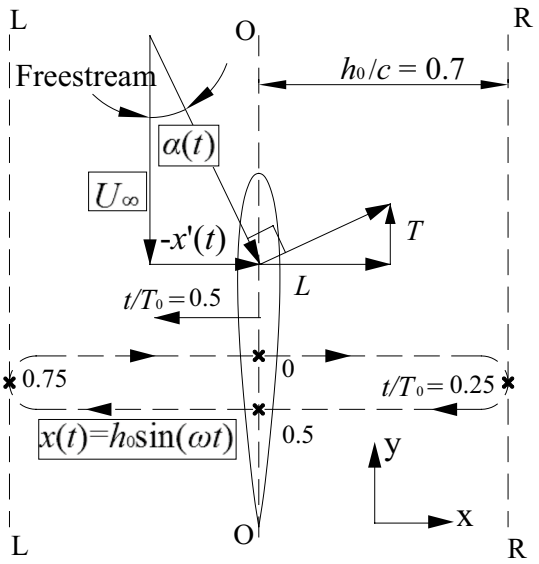

Fig. 2 Motion and force decomposition of a plunging wing. $\alpha(t)$ is the nominal angle of attack, $x(t) = h_0\sin(\omega t)$ is the kinematic equation of the plunging wing, T is the thrust, and L is the lift

$$c_l = \frac{\hat{L}(t)}{0.5\rho U_\infty^2 cs} \tag{6}$$

where s is the span length of the wing and $\hat{T}(t)$ and $\hat{L}(t)$ are the ensemble average thrust and lift of the forewing or hindwing in one plunging cycle.

3 Results and discussion

In the results, time (t) is normalized by the duration T_0 required to complete one plunging cycle motion. The instantaneous force on the wing, relative velocity vector field, relative streamlines, and vorticity contours around the forewing and the hindwing is demonstrated to discuss vortex interactions between the two wings. The frame of reference is fixed on the moving forewing or hindwing when the flow field is presented. The white arrow on the wing in flow field maps and the black in the schematic represents the wing motion direction. The arrow lengths indicate the relative magnitude of the plunging velocity. The absence of the white or black arrow implies that the plunging velocity of the wing is zero at that time.

3.1 Instantaneous lift and thrust on a single plunging wing

A comparison with a single wing under the same motion conditions is necessary to investigate the change in

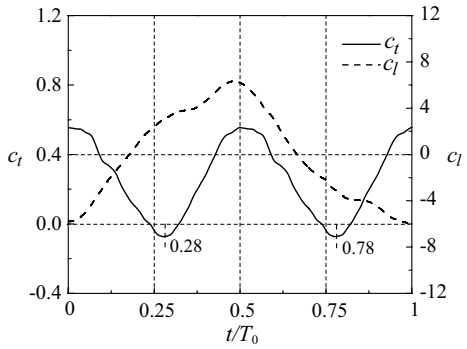

Fig. 3 Instantaneous thrust and lift coefficient of a single plunging wing

instantaneous thrust and lift on two plunging wings in tandem at different phase angles. The forewing is used as the single wing by moving the hindwing away. Figure 3 shows the instantaneous thrust and lift coefficients of a single wing. The maximum values of c_t and c_l occur at $t/T_0 = 0$ or 0.5, reaching up to 0.55 and 6.3, respectively. The minimum value of c_t is −0.07, which occurs at $t/T_0 = 0.28$ and 0.78.

3.2 Instantaneous force on the forewing

Gong et al. (2015) showed that the minimum and maximum values of the wing mean thrust correspond to phase angle $\varphi = 135$ and 315° at space distance 0.5 c, respectively. Therefore, the two typical phase cases are selected in the present study. In the following, it will be studied how the peak or magnitude value of the instantaneous thrust and lift is influenced by the phase angle and LEVs of the forewing and hindwing.

The instantaneous thrust c_t and lift c_l coefficients of the forewing at 135 and 315° are depicted in Fig. 4. They oscillate like a sinusoidal wave, similar to that of the single wing. The noticeable difference between the two cases lies in the variation in peak value of c_t or c_l near $t/T_0 = 0$ or 0.5. The peak value of c_t is 0.43 at 135° and 0.78 at 315°. The peak value of c_l is 5.17 at 135° and 8.17 at 315°. The forewing shows a low peak value of c_t or c_l at 135° and a high value at 315° compared with the single wing (Fig. 3). Lua et al. (2011) measured the lateral lift of a 2-D plunging wing in a water tank to simulate the hovering flight mode. Their peak lift reached 8.9, but the present single wing peak lift is 6.3. The peak lift slightly decreases in forward flight.

The nominal angle of attack $\alpha(t)$ of the plunging wing, as shown in Fig. 2, is defined as follows:

$$\alpha(t) = \arctan\left(\frac{h_0\omega\cos(\omega t)}{U_\infty}\right) \tag{7}$$

where ω is $2\pi f$. At $t/T_0 = 0$ or 0.5, the forewing passes through the equilibrium position with the largest plunging velocity. The maximum instantaneous lift or thrust is obtained when $\alpha(t)$ reaches maximum (Fig. 4). In reality, $\alpha(t)$ is generally not identical to the real effective angle of attack α_{eff}. In the present study, α_{eff} corresponds to the angle between the streamline and chord line (Fig. 5a). α_{eff} generally changes along the chord line and near the stagnation point arrives the maximum value. The variation of α_{eff} during a plunging cycle depends on the plunging velocity and the effect of the hindwing LEV. Figure 5a shows that the maximum α_{eff} is 63° at $\varphi = 135°$ and close to 90° at $\varphi = 315°$. For the plunging wing, the closer the maximum α_{eff} is to 90°, the greater the lift and thrust.

At the bottom right side of the forewing is a forewing-shed counterclockwise LEV (FW_CCW LEV) generated during the preceding half cycle (Fig. 5c). When the phase angle is 135°, a hindwing counter clockwise LEV (HW_CCW LEV) on the top left side of the hindwing has the same sense of rotation with the FW_CCW LEV. This HW_CW LEV restrains the jet-like flow around the forewing trailing edge (Fig. 5b, c), thereby decreasing the thrust of the forewing (Fig. 4a). The flow induced by HW_CCW LEV follows the same direction as the plunging velocity of the forewing and could impinge its leeward side, which decreases the maximum α_{eff}. Finally, a small lift is obtained (Fig. 4b). This phenomenon is the first type of vortex effect mechanism.

When the phase angle is 315°, a hindwing clockwise LEV (HW_CW LEV) on the top right side of the hindwing has an opposite sense of rotation with the FW_CCW LEV. The jet-like flow around the forewing trailing edge is enhanced by the HW_CW LEV (Fig. 5b, c), thereby increasing the thrust of the forewing compared with that of a single wing (Fig. 4a). The velocity induced by the HW_CW LEV on the windward side of the forewing follows the opposite direction of the plunging motion of the forewing (right portion of Fig. 5c); thus, the induced flow could impinge the windward side of the forewing. The relative velocity of the flow between the HW_CW LEV and the forewing on its windward side may increase, and accordingly the maximum α_{eff} rises. Thereby, a large lift is obtained (Fig. 4b). This phenomenon is the second type of vortex effect mechanism. Given the large plunging amplitude and small plunging frequency of the wing in the oncoming flow, the effect of the trailing edge vortex (TEV) is small and negligible.

Broering and Lian (2012) attributed the increase in peak value to the hindwing LEV. However, they did not provide information about the decrease in the peak value, as well as on how the hindwing LEV affects the flow field of the forewing. In the present study, the fluid dynamic mechanism of

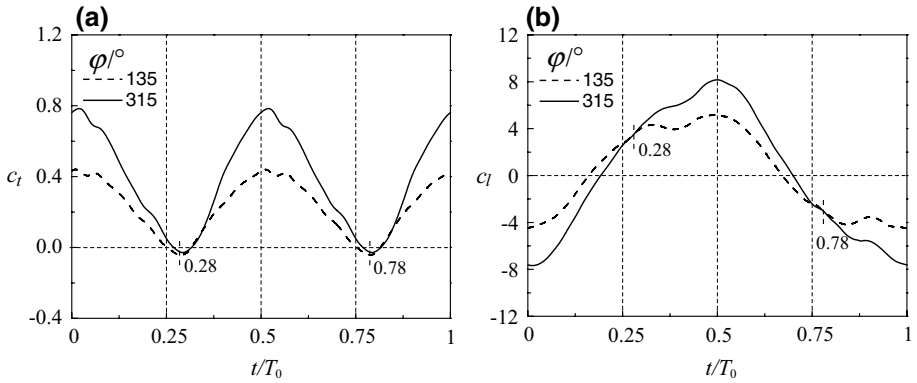

Fig. 4 Instantaneous thrust and lift coefficients of the forewing. **a** Thrust. **b** Lift

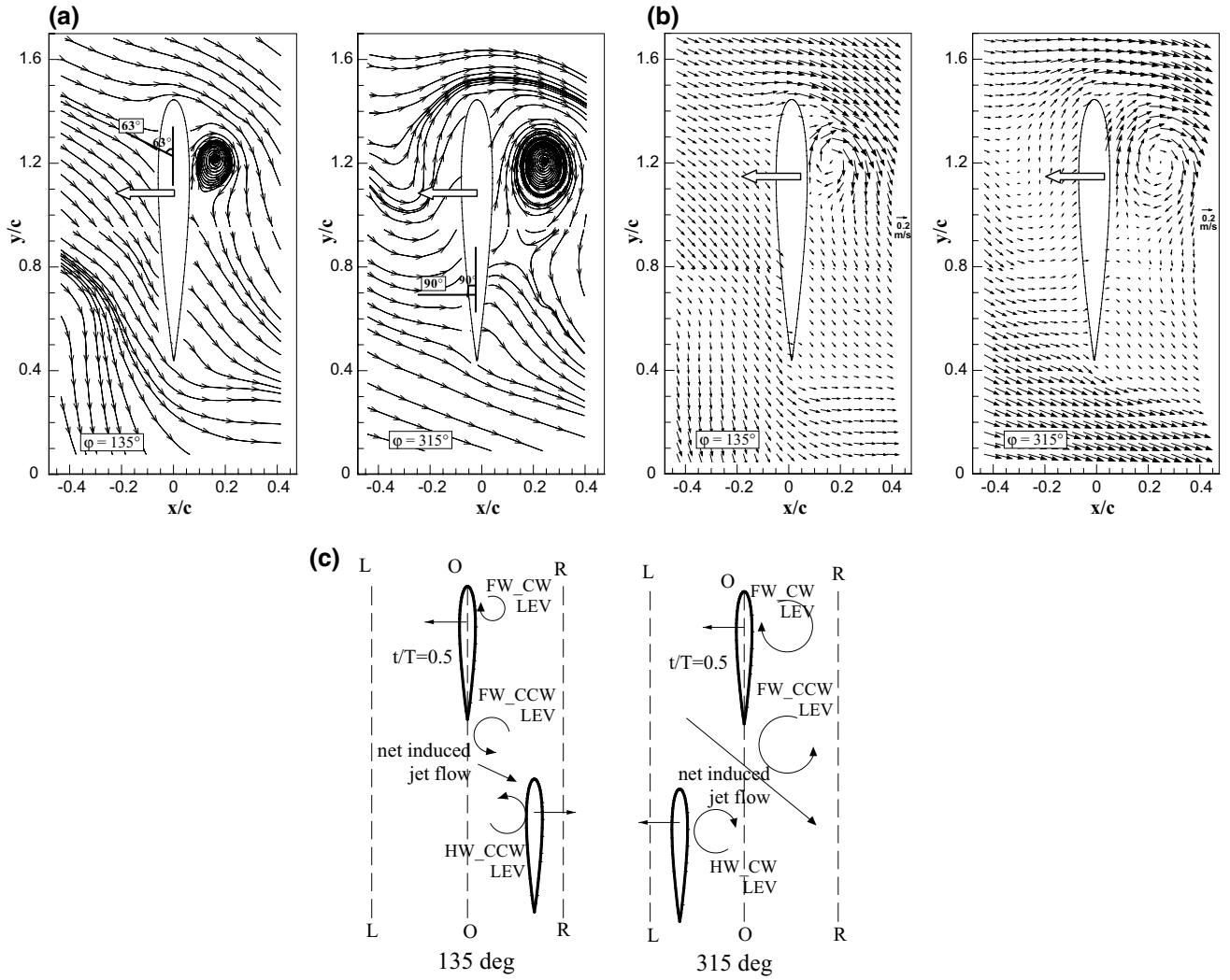

Fig. 5 Relative flow field with respect to a frame of reference fixed on the forewing at $t/T_0 = 0.50$. FW, HW, CW, and CCW denote the forewing, hindwing, clockwise, and counter clockwise rotations, respectively. **a** Relative streamlines around the forewing. **b** Relative velocity vector field around the forewing. **c** Schematic of the vortex interaction

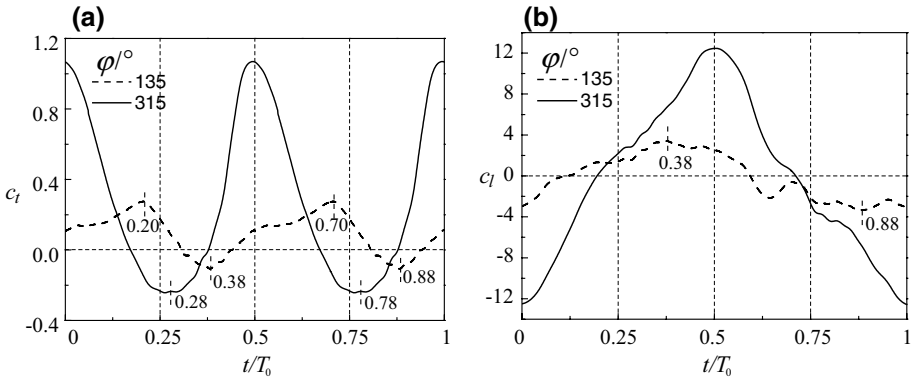

Fig. 6 Instantaneous thrust and lift coefficients of the hindwing. **a** Thrust coefficient. **b** Lift coefficient

the peak value increase or decrease in the forewing force is partially revealed.

3.3 Instantaneous force on the hindwing

The thrust c_t and lift c_l coefficients of the hindwing within a plunging cycle are illustrated in Fig. 6. The time $t/T_0 = 0.5$ indicates that the hindwing passes through the equilibrium position from right to left (Fig. 2). At $\varphi = 315°$, c_t reaches a peak value of approximately 1.06 at $t/T_0 = 0$ or 0.5 and a minimum value of approximately -0.23 at $t/T_0 = 0.28$ or 0.78, whereas c_l reaches a peak value of approximately ± 12.8 at $t/T_0 = 0$ or 0.5. At $\varphi = 135°$, c_t reaches a peak value of approximately 0.27 at $t/T_0 = 0.20$ or 0.70 and a minimum value of approximately -0.11 at $t/T_0 = 0.38$ or 0.88, whereas c_l reaches a peak value of approximately ± 3.47 at $t/T_0 = 0.38$ or 0.88. A large discrepancy is observed in the instantaneous force of the hindwing between the two phases, although the nominal angle of attack is identical at any time within a plunging cycle. This discrepancy may be attributed to the effects of the forewing-shed LEV on the flow field around the hindwing.

When $\varphi = 135°$ and $t/T_0 = 0.5$, the FW_CW LEV drifts to the top left side of the hindwing (left portion of Fig. 7a) and shifts the flow around the leading edge of the hindwing from right to left (left portion of Fig. 7b). The flow velocity relative to the hindwing decreases. This phenomenon is the first type of vortex effect described above. By contrast, when $\varphi = 315°$ and $t/T_0 = 0.5$, the FW_CCW LEV drifts to the top right side of the hindwing (right portion of Fig. 7a) and shifts the flow around the leading edge of the hindwing from left to right (right portion of Fig. 7b). The flow velocity relative to the hindwing increases. This phenomenon is the second type of vortex effect described above. Therefore, the maximum α_{eff} of the hindwing reaches about 62° at $\varphi = 315°$, which is much greater than that observed at $\varphi = 135°$, about 20° in Fig. 7b. The pressure difference between the pressure and suction sides of the hindwing increases at $\varphi = 315°$ and decreases at $\varphi = 135°$. These results agree with the ones obtained by Rival et al. (2010) for a single wing study. Consequently, at $t/T_0 = 0.5$, the hindwing has a larger value of thrust or lift for $\varphi = 315°$ than for $\varphi = 135°$ (Fig. 6).

In conclusion, the peak values of the instantaneous thrust and lift on the forewing and hindwing are greatly influenced by the interactions between the forewing-shed LEV and the LEV of the hindwing. Two types of vortex interactions are identified, and they depend on the phase angle. If the vortex interactions increase the oncoming flow velocity relative to the plunging wing, the peak lift and thrust increase. If the oncoming flow velocity decreases due to the LEVs interaction, the peak value drops.

3.4 Non-circulatory force contributions

The non-circulatory force contributions to the plunging wing lift and thrust are very important and may account for a large proportion in the total lift or thrust. Ford and Babinsky (2013) suggested that the lift on the impulsively started flat-plane aerofoil is caused by the external vortices and non-circulatory effects and indicated that the non-circulatory lift is responsible for almost half of the initial lift peak. By calculating the non-circulatory force on a plunging wing over a whole cycle and subtracting it from the measured lift and thrust, the measured force can be decomposed into circulatory force and non-circulatory force. This is helpful for improving the understanding of the lift and thrust generating mechanisms and especially the role played by the LEVs. Therefore, in the present paper the non-circulatory effect is taken into account.

The non-circulatory (added mass) force can be estimated by calculating the force on the flat plate accelerating in a stationary fluid and assuming that the flow is inviscid (Ford and Babinsky (2013). Usherwood and Ellington (2002) found that the force coefficients of the low Reynolds number ($Re \approx 8000$) propeller experiments are remarkably unaffected by considerable variations in leading-edge detail, twist, and camber. Therefore, for simplicity, a plate is used instead of a wing here.

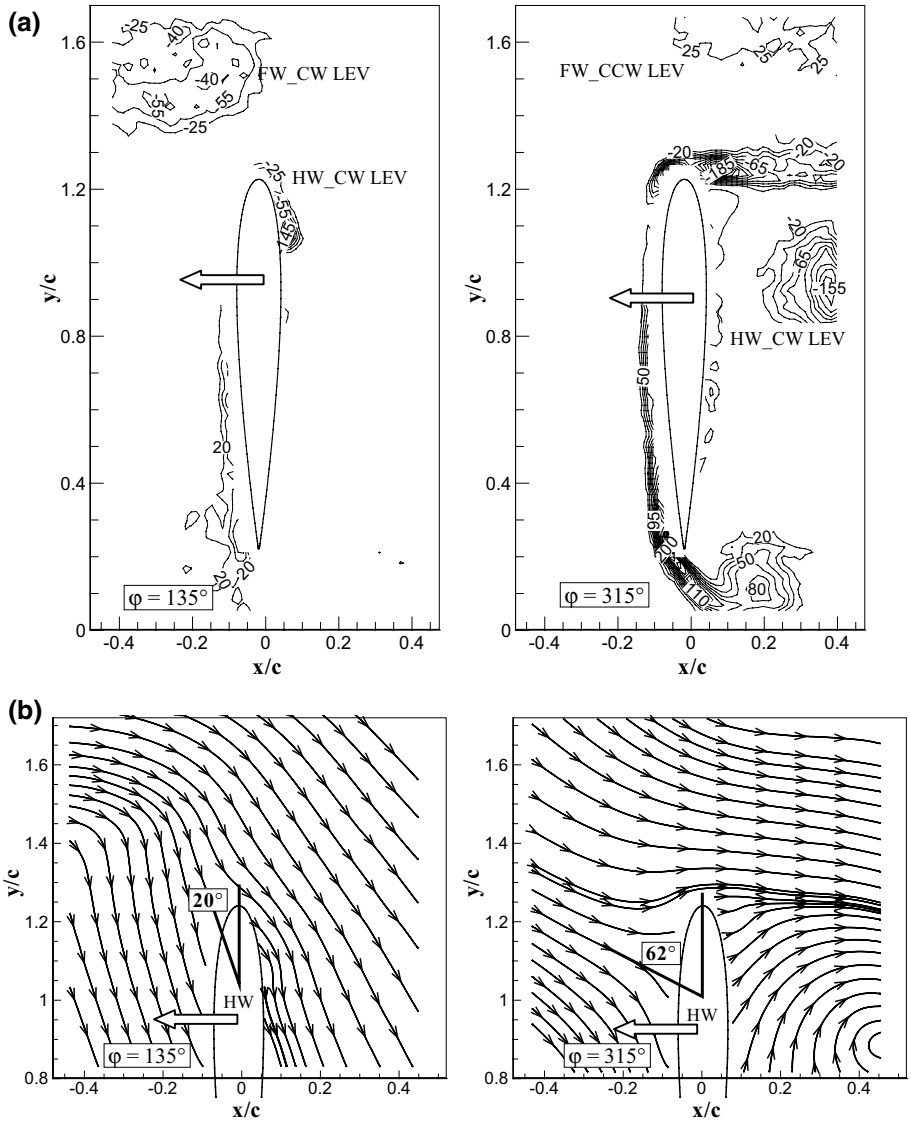

Fig. 7 Relative flow field with respect to a frame of reference fixed on the hindwing at $t/T_0 = 0.50$. **a** Vorticity Ω contours around the hindwing. **b** Relative streamlines around the hindwing

Using conformal mapping methods through an appropriate Kutta–Joukowski transformation applied to a circular cylinder of radius a in a flow, the transformation from the ζ-plane to the z-plane, where a flat plate is inclined at an angle of attack α to the oncoming flow, is represented by Ford and Babinsky (2013)

$$z = z_0 + \zeta + \frac{a^2}{\zeta} e^{-2i\alpha} \tag{8}$$

where z_0 is the complex coordinate of the center of a flat plate in the z-plane, as shown in Fig. 8.

Converting from a frame of reference in which the far-field flow is moving at velocity U to one in which the far-field flow is at rest, the complex potential in the ζ-plane $\bar{F}(\xi)$ becomes

$$\bar{F}(\xi) = U\frac{a^2}{\xi}\left(1 - e^{-2ia}\right) \tag{9}$$

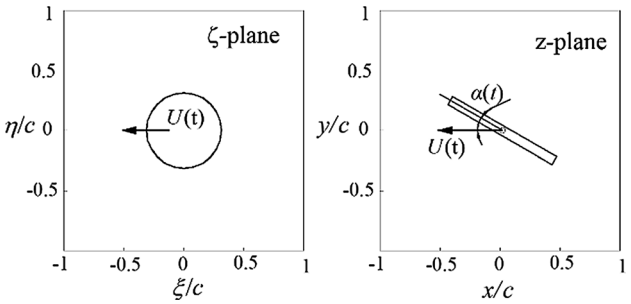

Fig. 8 Conformal mapping of the flow around a cylinder to the flow around a flat plate at angle of attack α(t)

The LEV and bound circulation around the cylinder are not considered in calculating the non-circulation force. According to the Blasius theorem, the force on a 2-D body

in an incompressible potential flow field is expressed as follows (Minotti 2002):

$$F_x - iF_y = i\frac{1}{2}\rho \int_{\text{body}} \left(\frac{\partial F}{\partial z}\right)^2 \mathrm{d}z - i\rho \frac{\partial}{\partial t}\left[\int_{\text{body}} F \mathrm{d}z\right] = i\frac{1}{2}\rho \int_{\text{body}} \left(\frac{\partial \bar{F}}{\partial \xi}\right)^2 \frac{\mathrm{d}\xi}{\mathrm{d}z}\mathrm{d}\xi - i\rho \frac{\partial}{\partial t}\left[\int_{\text{body}} \bar{F}\frac{\mathrm{d}z}{\mathrm{d}\xi}\mathrm{d}\xi\right] \tag{10}$$

where F is the complex potential in the z-plane. The steady integral is zero. The unsteady integral is given by

$$\int_{\text{body}} \bar{F}\frac{\mathrm{d}z}{\mathrm{d}\xi}\mathrm{d}\xi = Ua^2(1 - \mathrm{e}^{-2i\alpha})2\pi i \tag{11}$$

Then, the force is expressed as follows:

$$F_x - iF_y = 2\pi\rho a^2 \frac{\mathrm{d}\left(U(1 - \mathrm{e}^{2i\alpha})\right)}{\mathrm{d}t} \tag{12}$$

where

$$U(t) = \sqrt{U_\infty^2 + (h_0\omega\cos(\omega t))^2} \tag{13}$$

$$a(t) = \arctan\left(\frac{h_0\omega\cos(\omega t)}{U_\infty}\right) \tag{14}$$

Equation (12) is split into real and imaginary parts as follows:

$$F_x = 2\pi\rho a^2\left[(1 - \cos(2\alpha))\frac{\mathrm{d}U}{\mathrm{d}t} + 2U\sin(2\alpha)\frac{\mathrm{d}\alpha}{\mathrm{d}t}\right] \tag{15}$$

$$F_y = 2\pi\rho a^2\left[\sin(2\alpha)\frac{\mathrm{d}U}{\mathrm{d}t} + 2U\cos(2\alpha)\frac{\mathrm{d}\alpha}{\mathrm{d}t}\right] \tag{16}$$

The thrust T and lift L in the present study are defined as forces parallel and normal to the flat plate surface, respectively. Therefore, the non-circulatory forces on account of added mass attribute to the thrust and lift, and their contributions are expressed as follows:

$$\overline{L} = F_y\cos\alpha + F_x\sin\alpha \tag{17}$$

$$\overline{T} = F_y\sin\alpha - F_x\cos\alpha \tag{18}$$

Using Eqs. (17) and (18), the added mass force coefficients are calculated and shown in Fig. 9. The non-circulatory lift and thrust behave like sine curves. The thrust achieves its peak value of ± 1.0 at $t/T_0 = 0.16$ and 0.34; the lift has the peak value of ± 2.71 at $t/T_0 = 0.25$ and 0.75. The zero points of the thrust and lift curves are clear. Comparing Fig. 9 with Figs. 4 and 6, it can be seen that the peak value of the non-circulatory thrust is roughly equal to the measured total thrust peak at 315°, and more than twice at 135°. The peak value ratio of the non-circulatory to the measured lift at $\varphi = 135°$ is about 52.4 % for the forewing and 78.1 % for the hindwing; when $\varphi = 315°$, it is about 33.2 % for the forewing and 21.2 % for the hindwing.

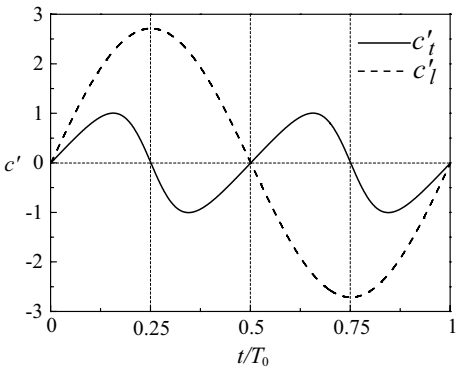

Fig. 9 Non-circulatory lift c_l' and thrust c_t' on account of added mass

Subtracting the corresponding added mass force from the measured results in Figs. 3, 4, and 6, the remainders are shown in Fig. 10, indicating the total contributions of the external vortices, bound circulation, and pressure drag caused by the flow separation and viscous effect.

For the forewing (Fig. 10a), the thrust c_t at $\varphi = 315°$ is slightly higher than that at $\varphi = 135°$. The main reason for the differences may be attributed to the effect of hindwing LEV, as discussed in Sect. 3.2. The single wing c_t in Fig. 10a is almost exactly between the two curves. The location of the minimum and maximum of the thrust in Fig. 10a is nearly the same as that of the maximum and minimum of the non-circulatory thrust in Fig. 9, respectively. For the forewing lift (Fig. 10b), the curve is symmetric at about $t/T_0 = 0.5$ and the zero points are exactly at $t/T_0 = 0.25$ and 0.75. This finding is greatly different from that in Fig. 4b. This difference is attributed to the added mass lift, as shown in Fig. 9.

For the hindwing (Fig. 10c), the peak thrust at $\varphi = 315°$ is approximately 1.60, much larger than the value of 0.96 at $\varphi = 135°$. The peak lift is also greatly higher than that at $\varphi = 135°$. This may be attributed to the effect of the forewing-shed LEV, as discussed in Sect. 3.3. The lift curve is symmetric at about $t/T_0 = 0.5$, and the zero points are almost exactly at $t/T_0 = 0.25$ and 0.75. This result is different from that in Fig. 6b. The difference comes from the added mass lift.

4 Conclusions

Experiments were conducted in a low *Re* water tunnel for two tandem wings in a 2-D plunging motion. A 3-D force sensor and a 2-D DPIV system were used to measure the instantaneous force on the two tandem wings, as well as the velocity field and LEV, respectively.

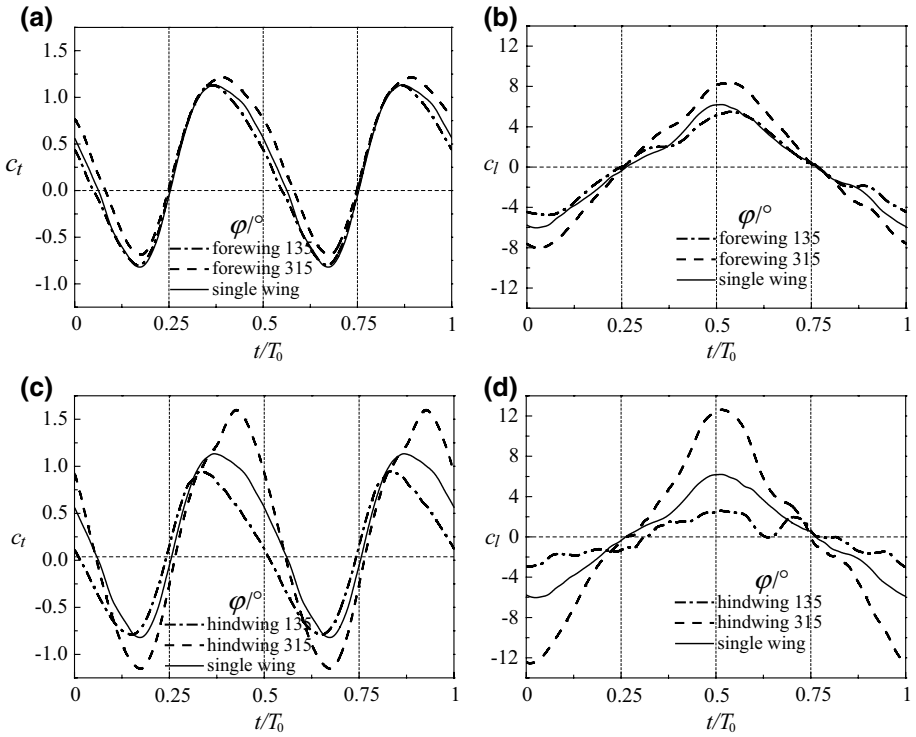

Fig. 10 Measured force subtracted by the added mass force. **a** Thrust of the forewing. **b** Lift of the forewing. **c** Thrust of the hindwing. **d** Lift of the hindwing

The influence of the phase angle and LEV on the peak value of the instantaneous thrust and lift is studied. The wing–wing interaction can either enhance or reduce the lift and thrust depending on the phase angles, but essentially on the sign of the forewing-shed LEV and the LEV of the hindwing. When the forewing-shed LEV encounters the hindwing and has a sense of rotation that is opposite to that of the hindwing LEV, it can generate a high oncoming flow, increase the maximum effective angle of attack, and enhance the instantaneous lift and thrust of the forewing and hindwing. When the two vortices have the same sense of rotation, a low oncoming flow is generated, thereby reducing the lift and thrust.

The non-circulatory effect has an important influence on the lift and thrust of plunging wings. For the tandem wing configuration studied here, the peak value of non-circulatory thrust is roughly equal to the measured thrust peak of the hindwing at 315°, and more than twice at 135° the peak value ratio of the non-circulatory to the measured lift for the forewing changes from 33.2 to 52.4 %. For the hindwing, the ratio ranges from 21.2 to 78.1 %. The non-circulatory lift mainly accounts for the measured lift at the peak deviation. The non-circulatory effect may greatly change the symmetry of the instantaneous lift and thrust curves.

Acknowledgments This work was supported by the National Natural Science Foundation of China (Nos. 50676072, 5123006). The authors also acknowledge the constructive feedback provided by the reviewers.

References

Akhtar I, Mittal R, Lauder GV, Drucker E (2007) Hydrodynamics of a biologically inspired tandem flapping foil configuration. Theor Comp Fluid Dyn 21(3):155–170

Alexander DE (1984) Unusual phase relationships between the forewings and hindwings in flying dragonflies. J Exp Biol 109(1):379

Anderson JM, Streitlien K, Barrett DS, Triantafyllou MS (1998) Oscillating foils of high propulsive efficiency. J Fluid Mech 360(1):41–72

Broering TM, Lian Y (2012) The effect of phase angle and wing spacing on tandem flapping wings. Acta Mech Sinica-prc 28(6):1557–1571

Broering TM, Lian Y, Henshaw W (2010) Numerical study of two flapping airfoils in tandem configuration. In: 48th AIAA aerospace sciences meeting including the new horizons forum and aerospace exposition

Broering TM, Lian Y, Henshaw W, Abate G (2012) Numerical investigation of energy extraction in a tandem flapping wing configuration. AIAA J 50(11):2295–2307

Dong H, Liang Z (2010) Effects of ipsilateral wing-Wing interactions on aerodynamic performance of flapping wings. In: Proceedings of 48th AIAA aerospace sciences meeting including the new horizons forum and aerospace exposition

Ford CWP, Babinsky H (2013) Lift and the leading-edge vortex. J Fluid Mech 720:280–313

Gong WQ, Jia BB, Xi G (2015) An experimental study on mean thrust of two plunging wings in tandem. AIAA J 53(6):1693–1705

Jones KD, Platzer MF (1997) Numerical computation of flapping-wing propulsion and power extraction. In: AIAA paper 97(826)

Lehmann FO (2008) When wings touch wakes: understanding locomotor force control by wake wing interference in insect wings. J Exp Biol 211(2):224–233

Lian Y, Broering T, Hord K, Prater R (2014) The characterization of tandem and corrugated wings. Prog Aerosp Sci 65:41–69

Lua KB, Lim TT, Yeo KS (2011) Effect of wing-wake interaction on aerodynamic force generation on a 2d flapping wing. Exp Fluid 51(1):177–195

Maybury WJ, Lehmann FO (2004) The fluid dynamics of flight control by kinematic phase lag variation between two robotic insect wings. J Exp Biol 207(26):4707–4726

Minotti FO (2002) Unsteady two-dimensional theory of a flapping wing. Phys Rev E 66:0519075

Platzer MF, Jones KD, Young JS, Lai JC (2008) Flapping wing aerodynamics: progress and challenges. AIAA J 46(9):2136–2149

Rival D, Manejev R, Tropea C (2010) Measurement of parallel blade–vortex interaction at low Reynolds numbers. Exp Fluid 49(1):89–99

Saharon D, Luttges MW (1987) Three-dimensional flow produced by a pitching-plunging model dragonfly wing. In: 25th AIAA aerospace sciences meeting

Saharon D, Luttges MW (1988) Visualization of unsteady separated flow produced by mechanically driven dragonfly wing kinematics model. In: 26th AIAA aerospace sciences meeting

Saharon D, Luttges MW (1989) Dragonfly unsteady aerodynamics: the role of the wing phase relationship in controlling the produced flow. In: 27th AIAA aerospace sciences meeting

Sun M, Lan SL (2004) A computational study of the aerodynamic forces and power requirements of dragonfly (Aeschna juncea) hovering. J Exp Biol 207(11):1887–1901

Taylor GK, Nudds RL, Thomas A (2003) Flying and swimming animals cruise at a Strouhal number tuned for high power efficiency. Nature 425(6959):707–711

Usherwood JR, Ellington CP (2002) The aerodynamics of revolving wings - I. Model hawkmoth wings. J Exp Biol 205(11):1547–1564

Usherwood JR, Lehmann FO (2008) Phasing of dragonfly wings can improve aerodynamic efficiency by removing Swirl. J R Soc Interface 5(28):1303–1307

Wang ZJ, Russell D (2007) Effect of forewing and hindwing interactions on aerodynamic forces and power in hovering dragonfly flight. Phys Rev Lett 99(14):148101

Wang H, Zeng L, Liu H, Yin C (2003) Measuring wing kinematics, flight trajectory and body attitude during forward flight and turning maneuvers in dragonflies. J Exp Biol 206(4):745–757

Warkentin J, DeLaurier J (2007) Experimental aerodynamic study of tandem flapping membrane wings. J Aircraft 44(5):1653–1661

Yamamoto M, Isogai K (2005) Measurement of unsteady fluid dynamic forces for a mechanical dragonfly model. AIAA J 43(12):2475